

30  
12-8-88

3T

①

CONF-880687--6

SLAC-PUB--4647

DE89 003787

# RF BREAKDOWN STUDIES IN ROOM TEMPERATURE ELECTRON LINAC STRUCTURES\*

GREGORY A. LOEW AND J. W. WANG

Stanford Linear Accelerator Center, Stanford University, Stanford, California 94309

## Introduction

This paper is an overall review of studies carried out by the authors and some of their colleagues on RF breakdown, Field Emission and RF processing in room temperature electron linac structures. The motivation behind this work is twofold: in a fundamental way, to contribute to the understanding of the RF breakdown phenomenon, and as an application, to determine the maximum electric field gradient that can be obtained and used safely in future  $e^+$  linear colliders. Indeed, the next generation of these machines will have to reach into the TeV ( $10^{12}$  eV) energy range, and the accelerating gradient will be one of the crucial parameters affecting their design, construction and cost. For a specified total energy, the gradient sets the accelerator length, and once the RF structure, frequency and pulse repetition rate are selected, it also determines the peak and average power consumption. These three quantities are at the heart of the ultimate realizability and cost of these accelerators.

Recent overall parameter studies for a 1 TeV  $e^+$  linear collider<sup>1</sup> indicate that accelerating gradients on the order of 100 to 200 MV/m are desirable and that the range of frequencies wherein such gradients would be affordable is 10 to 20 GHz. On the basis of the work reported here, it now appears that such performance is possible, at least in short and simple disk-loaded structures. Considerable insight has been gained into the mechanisms surrounding the complex and still elusive breakdown phenomenon. As will be seen, however, more work is needed to gain further understanding into the underlying physics, to determine if the required gradients are achievable in long and complicated structures, and to verify that the accompanying field emitted currents which can absorb power, cause parasitic wakefields and spurious x-rays along the accelerator, are tolerable.

## Accelerating Structures Tested

All experiments reported here, except for one that was started recently and is still incomplete, were performed on resonant standing-wave structures consisting of one or a few cavities. The use of such structures was made necessary by the present unavailability of the extremely high peak power sources that will eventually be required (500 to 1000 MW/m). The accelerating gradient in a short standing-wave section of length  $\ell$ , shunt impedance per unit length  $r_{sw}$ , and peak input power  $P$  is given by

$$E = \sqrt{\frac{P}{\ell} r_{sw}} \quad (1)$$

whereas for a corresponding traveling-wave section, it is

$$E = \sqrt{2\tau \frac{P}{\ell} r_{tw}} \quad (2)$$

valid for  $\tau \ll 1$ , where  $\tau$ , the attenuation of the section, is given by  $\omega\ell/2v_g Q$  and  $r_{tw}$ , the traveling-wave shunt impedance, differs from  $r_{sw}$  by at most a factor of 2. It is in principle possible to increase  $r$  for a short section of length  $\ell$  by decreasing the group velocity  $v_g$  to raise the stored energy density (typically by reducing the size of the irises). However, the structure would then no longer be representative of the ultimate accelerator design. Standing-wave tests were done at S-, C- and X-band at SLAC<sup>2,3,4</sup> and at Varian<sup>5,6</sup>, and tests on a traveling-wave structure, also at X-band, were recently begun in connection with the relativistic klystron program<sup>7</sup> carried out by SLAC in collaboration with LBL and LLNL.

\*Work supported by the Department of Energy, contract DE-AC03-76SF00515.

The first series of S-band tests was done with a seven-cavity resonant section of SLAC  $2\pi/3$ -mode constant-gradient structure. The structure can be seen in cross section in Fig. 1 and complete with its water cooling system in Fig. 2.

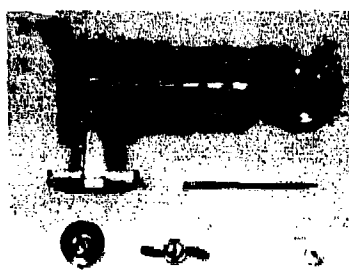


Fig. 1. Collection of S-band (seven-cavity,  $2\pi/3$ -mode), C-band and X-band cavities used in tests.

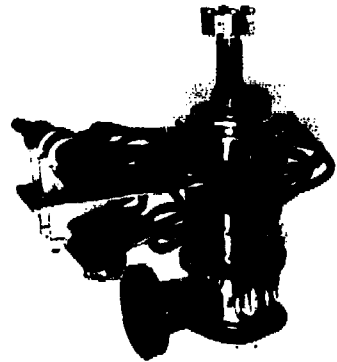


Fig. 2. S-band (seven-cavity,  $2\pi/3$ -mode) structure, complete with water cooling system.

It was supplied with RF from a 47 MW peak power XK-5 klystron with a 2.5  $\mu$ sec pulse width at 60 pps. The second series of S-band tests was done with a specially built  $\pi$ -mode two-cavity structure with nose cones. Their presence increased the ratio of peak-to-accelerating field, thereby reducing the required peak power from the above klystron to about 10 MW. Such a structure, with one RF feed per wavelength, was proposed by one of the authors<sup>8</sup> to circumvent the need for extremely high peak power. It is shown in Fig. 3. The C- and X-band cavities are shown in Figs. 1 and 4. To simplify the tests, only half-cavities were used in those cases. The experiments were carried out at Varian with ~ 1 MW magnetrons. Finally, preliminary tests have been done with a  $2\pi/3$  mode thirty-cavity traveling-wave structure at 11.424 GHz. Individual cavities can be seen in the lower right hand corner of Fig. 1. Short (10 to 25 nsec) pulses of 60 to 200 MW peak power from a six-cavity relativistic klystron were used to drive the section.

# MASTER

DISTRIBUTION OF THIS DOCUMENT IS UNLIMITED



Fig. 3. S-band (two-cavity,  $\pi$ -mode) structure, complete with water cooling system.

The repetition rate, however, was only 1 pps, and no clearly measurable breakdown was reached as this report is going to press. In all cases, standing-wave, and equivalent traveling-wave, accelerating and surface fields were calculated using the SUPERFISH computer program. The results are summarized in Table 1.

All experimentally measured maximum gradients for standing-wave structures are summarized in Table 2 for pulse lengths as shown. For the S-band tests, pulse length changes between 1.5 and 2.5  $\mu$ sec did not have a significant effect. The peak surface electric fields are plotted as a function of frequency in Fig. 5. A rough fit to this curve is

$$E_s \sim 195 [f \text{ (GHz)}]^{1/2} \quad (3)$$

Table 1. Fields calculated for normalizing condition

$$|\int_0^L E_x(z) \exp\{j(\omega z/c)\} dz|/L = 1 \text{ MV/m.}$$

	S-band		C-band	X-band	
	Disk-loaded ( $2\pi/3$ -mode)	With nose cone ( $\pi$ -mode)	Half-cavity*	Half-cavity*	Disk-loaded ( $2\pi/3$ -mode)
Frequency, $f$ (MHz)	2856.0	2856.38	4998.0	9346.5	11423.7
Length for calculation, $L$ (cm)	5.2485	5.2485	1.507	0.806	1.3121
Beam hole diameter, $2a$ (cm)	1.99	1.6	0.748	0.40	0.75
Factor of merit, $Q$	13,798	18,489	70.8	5595	6960
Shunt impedance (M $\Omega$ /m)	62.8/2	74.2	79.6	88.83	98.0
Energy stored, $W$ (J)	$1.239 \times 10^{-3}$	$7.254 \times 10^{-4}$	$3.951 \times 10^{-5}$	$7.205 \times 10^{-5}$	$2.5415 \times 10^{-5}$
Power dissipated, $P_D = \omega W/Q$ (W)	1611.7	704.12	176.8	75.26	262.07
Average accelerating field $\bar{E}_{acc}$ (MV/m)	0.9815	0.9077	0.966	0.9087	0.9893
Maximum axial field at $z = 0$ , $ E_{x,SW} _{max}$ (MV/m)	2.692	1.8655	3.1683	2.0212	1.616
Maximum surface field, $ E_{s,SW} _{max}$ (MV/m)	4.263	4.145	7.54**	4.876	4.602
$ E_{s,SW} _{max} / \bar{E}_{acc}$	2.742	1.87	3.28	2.224	1.633
$ E_{o,SW} _{max} / \bar{E}_{acc}$	4.342	4.15	7.81	5.37	4.55

\*For half-cavities with end-plate,  $r$  and  $Q$  are lower than they would be for a full cavity.

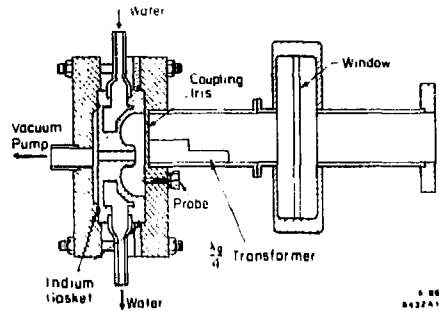


Fig. 4. Cross-sectional view of demountable C-band cavity.

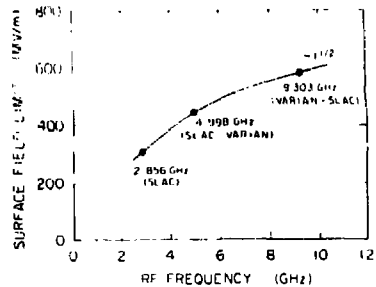


Fig. 5. Peak breakdown surface fields measured as a function of frequency.

Table 2. Experimentally obtained gradients.

	S-band		C-band	X-band	
	Disk-loaded ( $2\pi/3$ -mode)	With nose cone ( $\pi$ -mode)	Half-cavity	Half-cavity	Disk-loaded ( $2\pi/3$ -mode)
Frequency, $f$ (MHz)	2856	2858	4998	9303	11424
Total length (cm)	24.5	10.5	1.507	0.806	26.25
Filling time* ( $\mu$ s)	0.77	1.0	0.172	0.082	0.028
Pulse length ( $\mu$ s)	1.5-2.5	1.5-2.5	3.5	3.8	0.025 <sup>†</sup>
Peak power input (MW)	~ 47	~ 10	0.8	1.2	200 <sup>†</sup>
Peak surface field, $E_s$ (MV/m)	312	340	445	572	305 <sup>†</sup>
Corresponding traveling-wave accelerating field <sup>‡</sup>	144	157	205	267	140 <sup>†</sup>

\*For critical coupling in the case of standing-wave structures.

<sup>†</sup>Preliminary results.

<sup>‡</sup>Assuming SLAC structure, working in the traveling-wave mode, in which  $E_s/\bar{E}_{acc} = 2.17$ .

We see that if this empirical relationship is valid at the higher frequencies such as four times SLAC (11.424 GHz) or six times SLAC (17.136 GHz) which are presently being considered, we could expect the breakdown limits shown in Table 3.

Table 3. Predicted limiting gradients for future colliders at specific frequencies.

Extrapolated Limiting Gradients	11.424 GHz	17.136 GHz
Peak Surface Field (MV/m)	660	807
Accelerating $E_s/\bar{E}_{acc}$ (MV/m) assuming $E_s/\bar{E}_{acc} = 2.5$	264	323

assuming no improvements due to the much shorter pulse lengths required at the higher frequencies (~ 20 to 100 nsec), and conversely no worsening due to the probable need for more complex structures with higher-order modes and slots in the disks.<sup>9</sup>

We will now discuss the details of the experimental conditions under which the above results were obtained.

#### Experimental Setups and Conditions

Since the inception of these tests in 1984, just about four years ago, the experimental setup used for the S-band tests has been gradually modified to refine the measurements and allow different observations. Two typical setups are shown in Figs. 6 and 7 for the  $2\pi/3$  and  $\pi$ -mode sections, respectively. Both these tests were done inside a concrete vault in the SLAC Cryogenics Building. This vault consists of three-foot thick shielding blocks and a complete radiation safety interlock system. The klystron, modulator and power supply are located on the roof of the vault and the microwave power is piped to the accelerator structure via a vertical rectangular waveguide whose vacuum is separated from the structure vacuum by a ceramic window.

In Fig. 6, the test points (1-4) were used to make temperature measurements in the copper walls and in the disk tips. The temperature increases tracked linearly with the average power dissipated in the cavities, and the highest temperatures were reached, as expected, in the disks (see Ref. 3).

The frequency to obtain resonance had to be tuned accordingly. The end-plates were originally made out of stainless steel but after an RF-focused field-emitted (FE) beam punctured the downstream plate, they were replaced by 1.25 cm thick copper plates, thinned down on axis to 0.38 mm thick, 1.4 cm diameter "windows" to permit extraction and analysis of the FE beam. Two internal probes with coaxial SMA feedthroughs were installed at both ends to monitor and measure internal FE currents. Subsequently, eight transverse coaxial SMA probes were installed (3A, 4A, etc. in the full-field cavity A, and 3B, 4B, etc. in the half-field cavity B),<sup>2</sup> also to measure FE currents, but this time to detect any azimuthal asymmetries in emission.

When the axially extracted FE currents became measurable, a bending magnet, momentum analyzing slit and Faraday cups were added at the down-stream end (right in Fig. 6). Later, this equipment and the downstream copper window were removed and a glass window, mirror and black-and-white video camera were installed in the shielding vault to look inside the section during high-gradient operation. An attempt was also made to use two color video cameras, but neither could be operated successfully: the first one because it was affected by x-ray radiation, and the second because of insufficient sensitivity. Dipole magnets were wrapped around the section and/or along an axial output pipe, to prevent FE electrons from melting the glass window. The effect of these magnets was to bend the electrons into the walls, but—in the process—to generate additional x-rays which produced a strong luminescent background glow as they passed through the glass window.

After the seven-cavity section was removed, the two-cavity section was installed in the same general location inside the vault and several additional experiments were performed. Figure 7 shows a detailed sketch of the vacuum system, two ion pumps, a cryo pump, a residual gas analyzer (RGA) and a leak valve to introduce various gasses into the cavity under controlled conditions. Ionization chambers were installed around the sections to measure the radiation levels, and at one point, a simple x-ray pinhole camera was constructed to detect transverse emission from the section. It revealed that at very high field levels, the disks were actually responsible for the highest transmission of x-rays.

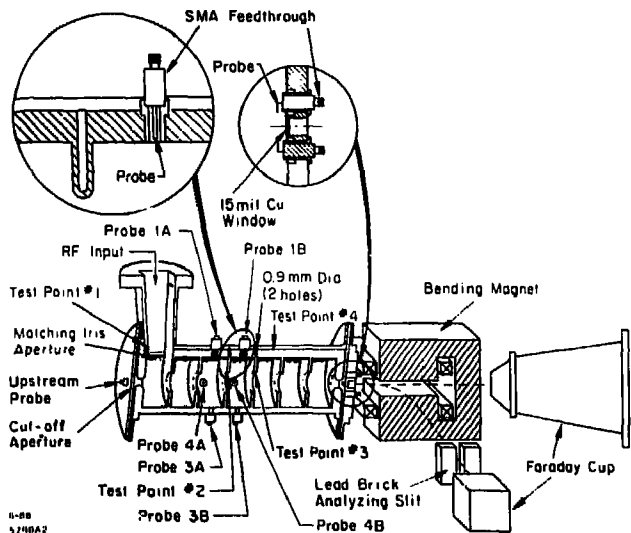


Fig. 6. Experimental set-up used for S-band (seven-cavity,  $2\pi/3$ -mode) structure.

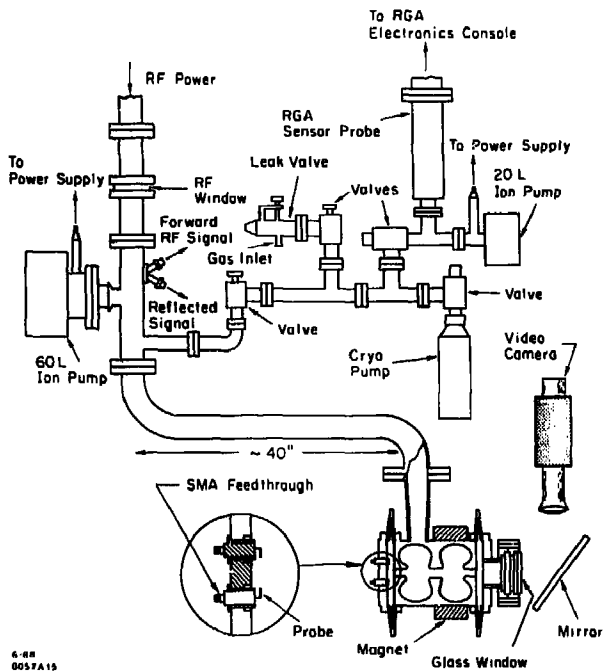


Fig. 7. Experimental set-up used for S-band (two-cavity,  $\pi$ -mode) structure, showing details of vacuum system.

## Chemical Cleaning and Baking

At various stages when the sections were removed from the experimental area and had to be machined, they were subsequently cleaned. The chemical procedure that was typically used is described in Table 4. The various steps that are listed were empirically developed by the Plating Shop at SLAC. Occasionally, the section was also baked at 250°C, principally to remove the water vapor from the inside surfaces. This procedure seemed well-suited to shorten the RF processing time.

Table 4. Procedure for chemical cleaning.

- Vapor degrease in trichlorethanes for five minutes
- Remove oxide by immersion in non-etch copper cleaner (citrate, McDermid 9268) at 100°F for five minutes
- Tap water rinse
- Immerse in OXYBAN 60 solution for two minutes
- Rinse in tap water, cold and hot de-ionized water
- Immerse in 115°F isopropyl alcohol for 15 seconds
- Blow with dry air
- Dry in hot air oven at 150°F for two hours

## Field Emission, Fowler-Nordheim Plots and the Kilpatrick Breakdown Limit

Since electron field emission (FE) is at the heart of the prebreakdown and breakdown phenomena, and the Fowler-Nordheim equation and plots are used by many different authors, it seems worthwhile to review here which form of the equation is used for RF fields in this paper and why.

In the case of DC fields, the FE current density in  $A/m^2$  given by FN is generally<sup>10</sup>

$$j_F = \frac{1.54 \times 10^{-6} \times 10^{4.52\phi^{-0.1}} E^2}{\phi} \exp \left\{ -\frac{6.53 \times 10^9 \times \phi^{1.5}}{E} \right\}, \quad (4)$$

where  $E$  is the externally applied field in  $V/m$  and  $\phi$  is the work function of the metal in eV.

In the case of RF fields, Eq. (4) is slightly modified and the average emitted current density becomes

$$\bar{j}_F = \frac{6 \times 10^{-12} \times 10^{4.52\phi^{-0.1}} E^{2.5}}{\phi^{1.75}} \exp \left\{ -\frac{6.53 \times 10^9 \times \phi^{1.5}}{E} \right\}. \quad (5)$$

If we now assume that the emitted current is the result of FE from an area  $A_E$  and that, because of some geometric irregularity, the field is enhanced by a factor  $\beta$ , the average FE current is given by

$$\bar{I}_F = \frac{6 \times 10^{-12} \times 10^{4.52\phi^{-0.1}} A_E (\beta E)^{2.5}}{\phi^{1.75}} \exp \left\{ -\frac{6.53 \times 10^9 \times \phi^{1.5}}{\beta E} \right\}, \quad (6)$$

where  $\beta$  is a field enhancement factor. In principle, this factor has a direct physical meaning only for metallic protrusion. If the shape of the protrusion is reasonably simple, its value of  $\beta$  can be calculated quite accurately. Experimentally, the

numerical value of  $\beta$  can be derived from plotting  $I_F/E^{2.5}$  versus  $1/E$  on semilog paper and using the expression for the slope:

$$\frac{d(\log_{10} I_F/E^{2.5})}{d(1/E)} = \frac{-2.84 \times 10^9 \phi^{1.5}}{\beta} \quad (7)$$

This is the expression that has been used throughout this paper. The zero-intercept for infinite field is proportional to  $\log_{10} A_E \beta^{2.5}$ .

As will be shown later, after many hours of cavity operation, the microprotrusions observed with a scanning electron microscope are highly irregular, but their height-to-top-radius ratio can at best explain values of  $\beta$  between 5 and 10. On the other hand, the measured values when steady-state in RF processing is reached, are on the order of 60. Thus, an additional mechanism<sup>11,12</sup> having to do with dielectric impurities is generally invoked (see below).

The breakdown limits shown in Fig. 5 and empirically expressed in Eq. (3) exceed by a factor of roughly seven the predictions of the Kilpatrick model.<sup>13</sup> This result is by now no longer unusual and has been obtained by numerous other accelerator workers. It is worthwhile to point out why this is not surprising. The Kilpatrick criterion is based on the idea that breakdown happens when regular FE is enhanced by a cascade of secondary electrons ejected from the cathode by ion bombardment. Assuming a linear dependence of secondary emission of electrons upon maximum ion energy, an expression for the breakdown or "sparking" threshold was obtained empirically from many experimental points, as:

$$WE^2 \exp\{-1.7 \times 10^6 E^{-1}\} = 1.8 \times 10^{14}, \quad (8)$$

where  $W$  is the maximum possible ion energy in eV and  $E$  is measured in  $V/cm$ . The maximum energy of an ion of mass  $M_0$  and charge  $z$ , calculated for a relatively large gap of parallel plates and taking into account the transit time, was found to be

$$W = \frac{(0.153 e E^2)}{M_0 \pi f^2}, \quad (9)$$

from which the Kilpatrick criterion was derived as

$$f = 1.64 E^2 \exp \left\{ -\frac{8.5}{E} \right\}, \quad (10)$$

with  $f$  measured in MHz,  $E$  in  $MV/m$  and the ion assumed to be hydrogen.

Upon examination, there are several discrepancies between the original assumption that went into the above empirical expression [Eq. (8)] and the present measurements. First of all, the original point at 2856 MHz that was given to Kilpatrick was  $E = 0.5$   $MV/cm$  (and not 3.4  $MV/cm$ ), corresponding to  $W = 1.5$  keV (as opposed to 53 keV for today's 3.4  $MV/cm$ ). By definition, our point cannot lie on the same curve. Second, the Kilpatrick formula for  $W$  was based on a gap of parallel plates which is quite different from the condition inside RF cavities with rounded disks and possible field enhancements due to microprotrusions, dielectric inclusions, etc. Finally, the multiplicative effect of  $W$  in Eq. (8) assumed that the avalanche of secondary electrons produced by ion collisions was the dominant cause of RF breakdown. With FE current densities as high as  $10^8$   $A/cm^2$ , it is improbable that ions ( $\sim 10^{10}$  hydrogen atoms/ $cm^3$  in a vacuum of  $10^{-6}$  Torr) can play a dominant role.

## Observations of Field Emission, RF Processing and RF Breakdown

We will now attempt to summarize our observations of field emission, RF processing and RF breakdown as we gathered them through our various tests. In the interest of succinctness and clarity, the chronological sequence described below is the result of combining the observations from several of the tests together.

1. Let us assume that we start with a reasonably well machined, high quality copper accelerator structure. It has been cleaned by the techniques described above, and possibly vacuum baked at 200 to 250°C for more than 24 hours. Surfaces appear to be smooth.
2. The structure is pumped down to  $\sim 10^{-8}$  Torr.
3. An RGA read-out exhibits a strong H line, weak C,  $\text{C}_2$ ,  $\text{CH}_2$ ,  $\text{CH}_3$ ,  $\text{CH}_4$ , HO lines, medium  $\text{H}_2\text{O}$  and  $\text{N}_2$ - $\text{CO}$ , and weak  $\text{CO}_2$ ; occasionally, also some  $\text{C}_2\text{H}_2$  (see Fig. 8a).
4. Pulses of gradually increasing RF power (2.5  $\mu\text{sec}$ -long) are applied to the structure, starting from about 2 MW

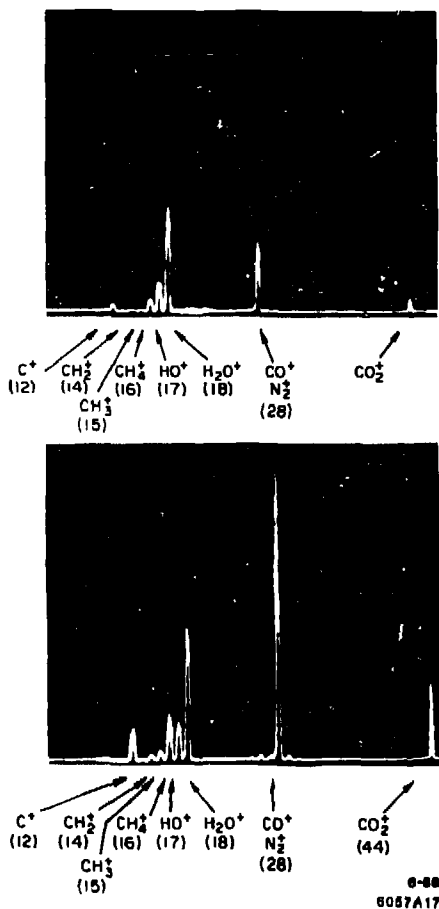


Fig. 8. Residual gas analyzer displays during RF processing of S-band, two-cavity structure, a) before breakdown, and b) immediately after breakdown.

peak. The power level corresponds to 80 MV/m peak in our seven-cavity structure or 170 MV/m in our two-cavity structure. Occasional RF breakdown is detected. Breakdown events are manifested by the following observations:

- (a) The reflected RF pulse jitters violently and the corresponding forward pulse from the source (klystron or magnetron) becomes somewhat erratic (see Figs. 9a,b).

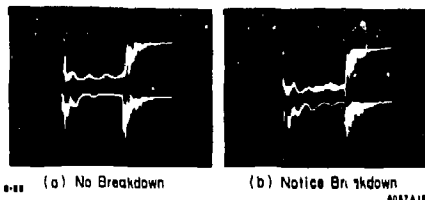


Fig. 9. Forward and reflected RF wave shapes: a) normal, b) during breakdown.

- (b) When a glass window is available, sparks are visible in high field areas, namely on disk edges, via the video monitor and recorder.
- (c) Whatever field emission (FE) current is observed at a given power level before breakdown, the current jumps instantaneously (i.e., within a few nanoseconds, in the pulse) by a factor of 20 to 30, as viewed on current probes or on an electrometer. When the breakdown stops, the FE current immediately returns to its pre-breakdown level.

A typical breakdown event is shown in Fig. 10. Such an event was recorded for the seven-cavity S-band structure (Fig. 6) by using a Camac Interface System to a VAX785 computer to digitize and store eight pulses produced at the instant of breakdown. More than 80 such events were recorded.

When a typical breakdown event takes place, predominantly in cavity (A), it is invariably picked up on all four probes in cavity (A), channels one, two, three and four, but does not spill over much into cavity (B), channels five and six. Arcing and gassing seem to expand throughout the cavity in all four directions. The seventh channel in Fig. 10 was connected to the probe upstream of the left-hand cut-off aperture, and the eighth channel to the forward RF pulse. The breakdown current in most recorded events appears after the first microsecond into the pulse, continues for about one microsecond after the end of the pulse while the structure is discharging, and frequently rebounds at a lower level, when the fields have practically died out. The latter phenomenon is not understood, but could be due to some form of multipactoring.

- (d) X-ray radiation bursts as observed on ion chambers alongside the structure also coincide with these pulses.
  - (e) The RGA exhibits temporary increases in all C-related lines (see Fig. 8b).
  - (f) The overall pressure increases to  $\sim 10^{-7}$  Torr.
5. These events generally last for only one RF pulse (2.5  $\mu\text{s}$ ) or sometimes two or three consecutive pulses, unless power is raised too fast, in which case the pressure can increase to  $10^{-5}$  Torr or higher, causing multiple breakdowns and impeding any further progress in RF processing. If the power is simply kept constant for a few minutes, the vacuum improves, C-related lines return to steady-state and gradual RF processing can resume.

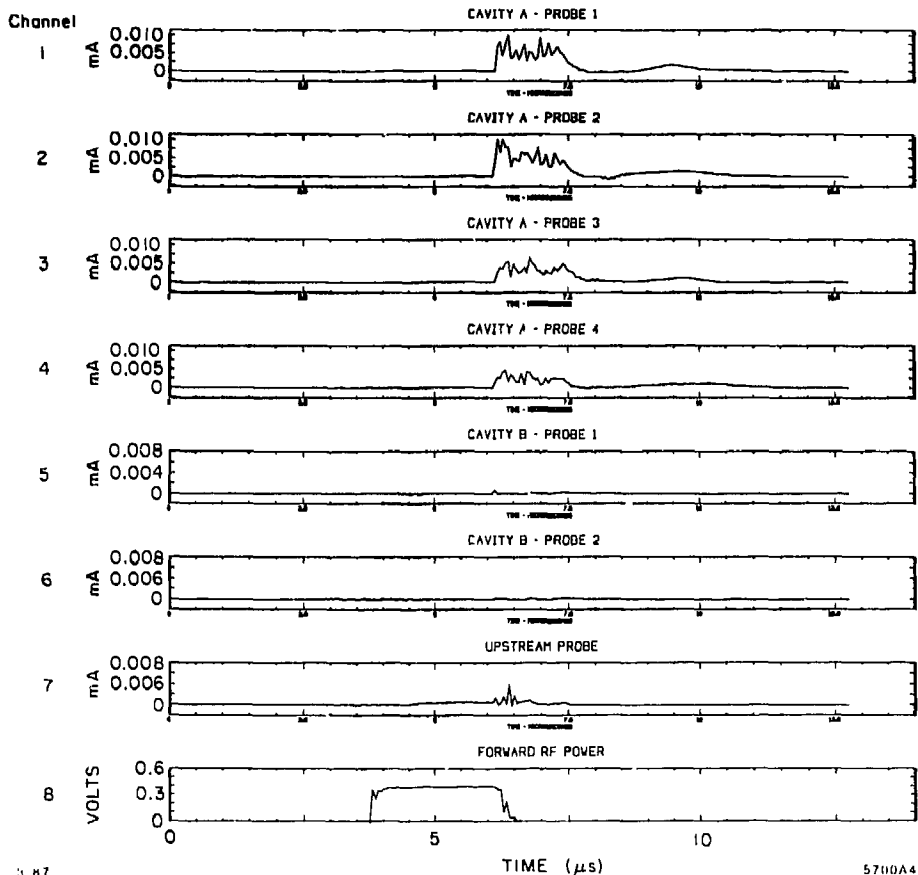


Fig. 10. Breakdown "event" recorded at four radial probes in full-field cavity (A), two radial probes in half-field cavity (B), and one upstream probe. The forward RF pulse provides a time reference.

6. Our observation is that this sequential pattern of breakdown, subsequent recovery and gradually increasing field repeats itself all the way up to the maximum field ( $\sim 340$  MV/m on the disks at S-band). With freshly constructed structures or structures processed earlier but exposed to air for several hours, this process has taken between three and fourteen hours (for a typical schedule, see Fig. 11). There seems to be no observable difference between the breakdown events in the range from 170 to 340 MV/m, except that the steady-state FE current increases as the field increases. Once the maximum field is reached (beyond which the cavity breaks down almost continuously), it is possible to decrease the power input and then instantaneously increase it back to its maximum value without any breakdown. If, after this, the structure is left under good vacuum ( $10^{-7}$  to  $10^{-8}$  Torr) for several days, the process takes only a few minutes. Under these conditions, repeatable data points for Fowler-Nordheim plots ( $i_{FE}/E^{2.5}$  versus  $1/E$ ) can be obtained. Field enhancement  $\beta$ -values of  $\sim 60$  have been measured over a wide range of conditions for S-band and  $\beta \sim 38$  for C-band (see Fig. 12).

7. In the case of the seven-cavity structure (see Fig. 6), an attempt was made to calculate and measure the trajectories, currents and energies of FE electrons accelerated and focussed by the RF fields. Typical trajectories are shown in Fig. 13, as calculated by the program NEWTRAJ,<sup>14</sup> and indicate how an intense beam can actually be generated everywhere inside the structure.

The cross-section of the FE beam was measured with a piece of cinemoid film placed on both upstream and downstream outside surfaces of the windows and found to be approximately 3 mm in diameter, almost independently of RF power level. The beam current transmitted through the downstream window was measured with the Faraday cup and found to reach 25 mA peak at 35 MW peak power, as shown in Fig. 14. By passing through the window, the electrons produce an electromagnetic shower and are scattered at various energies and angles. The relative beam current transmitted to the collector behind the slit formed by two lead bricks was measured as a function of the bending magnet setting between 0

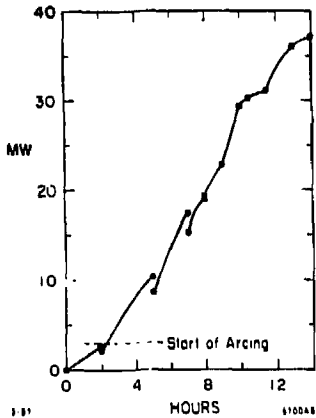


Fig. 11. Typical RF processing schedule for S-band, seven-cavity structure.

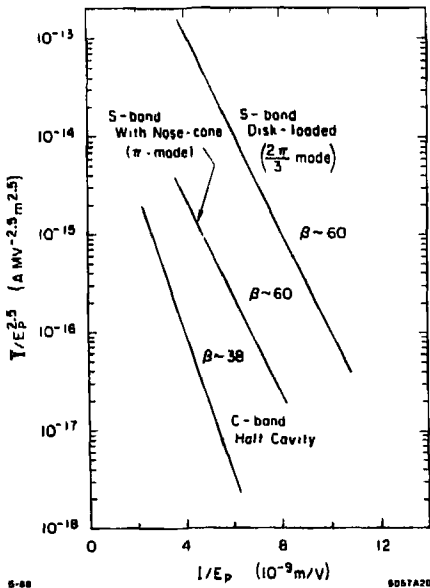


Fig. 12. Fowler-Nordheim plots for S-band and C-band structures.

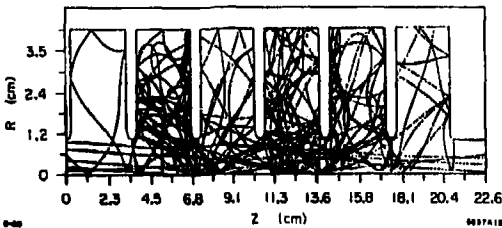


Fig. 13. Typical field emitted electron trajectories plotted for S-band ( $2\pi/3$ -mode) structure by means of computer program NEWTRAJ (courtesy of R. Parodi).

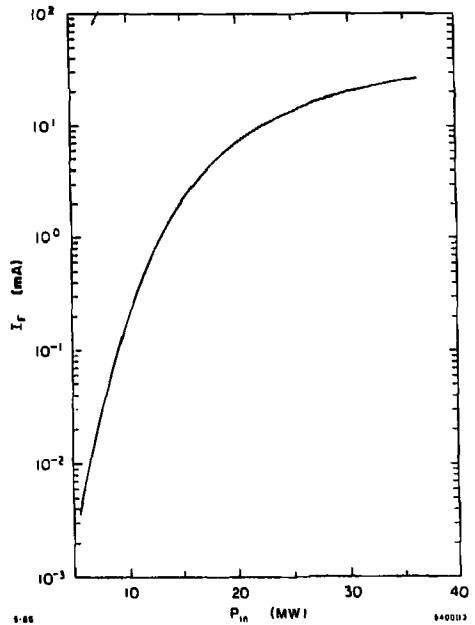


Fig. 14. Field emitted current transmitted through downstream window (right-hand side in Fig. 6) to Faraday cup, as a function of peak input power.

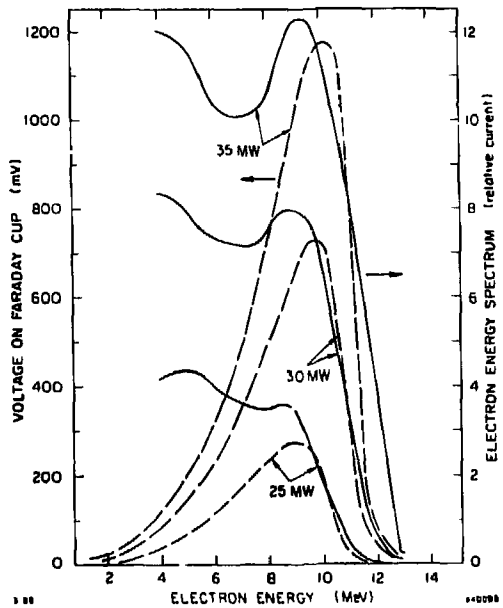


Fig. 15. Uncorrected (dashed lines) and corrected (continuous lines) electron energy spectra for various values of peak input power into S-band seven-cavity structure.

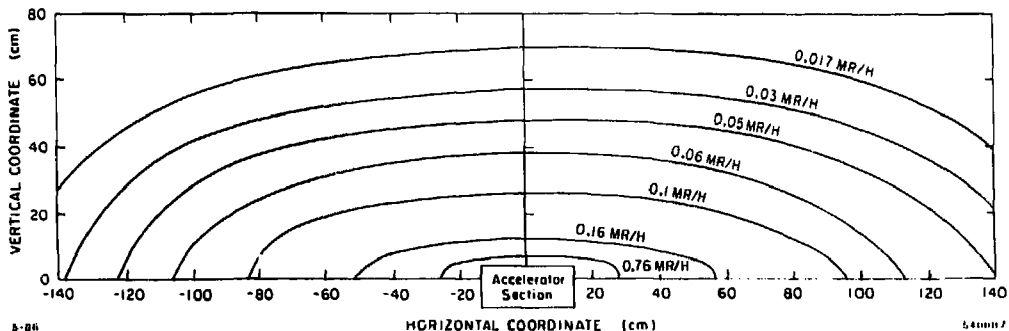


Fig. 16. Average x-ray dosage distribution around S-band (seven-cavity,  $2\pi/3$ -mode) accelerator section (300 MV/m surface field,  $2.5 \mu\text{sec}$ , 120 pps).

and 4000 G to give energy spectra for various power levels. These energy spectra had to be corrected for scattering through the window and gas scattering. This was done with the aid of the program EGS4 which simulates bremsstrahlung, electron-electron scattering, ionisation loss, pair production, photoelectric effect and multiple Coulomb scattering, and the TRANSPORT computer program. For each incident electron energy and corresponding magnetic field for maximum transmission through the slit, a ratio of current to the collector to current incident on the window could be obtained. This ratio was then used to renormalise the measured spectra at various power levels and obtain the actual electron spectra (Fig. 15). The double humps correspond to electrons captured in the third cavity and accelerated through the entire section or captured in the sixth cavity and accelerated to the output end.

The extremely elevated x-ray dosage distribution is shown in Fig. 16. A dosage curve as a function of peak electric field for the two-cavity  $\pi$ -mode structure is shown in Fig. 17.

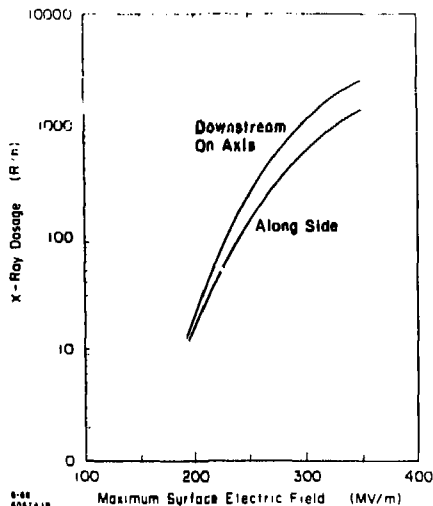


Fig. 17. Average x-ray dosage around S-band (two-cavity,  $\pi$ -mode) accelerator section ( $2.5 \mu\text{sec}$ , 60 pps) as a function of peak field.

- After completion of the tests, the disk edges in the structure exhibit numerous pits and crater-like holes, several tens of microns in diameter (see Fig. 18). The longer one has operated the structure, the more pits one finds. The number of pits does not seem to affect the breakdown level, but it probably increases the steady-state FE current. It shifts the Fowler-Nordheim plots up, but it does not change their slope from their typical value of  $\sim 60$ . Scanning electron microscope pictures of one particular disk also show drops of molten copper in areas of lower electric field and indicate that the pits and craters are the result of very high temperature eruptions.

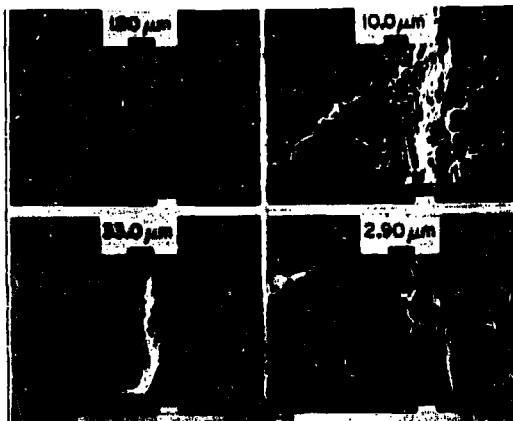


Fig. 18. Scanning electron microscope pictures of C-band cavity nose cone showing RF breakdown damage (note four successive scales in microns).

- Controlled exposure of the evacuated cavities ( $10^{-7}$  Torr) to gases was tried with CO and CO<sub>2</sub>. Exposure to 50 milli-Torr of CO for three minutes, followed by pump-down, had the temporary effect of increasing  $i_{FE}$  by about 30%, but RF processing for about 15 to 30 minutes lowered it back to its pre-exposure asymptotic value. A very similar experiment carried out subsequently with CO<sub>2</sub> had almost no effect at all.
- "RF scrubbing" with argon and helium was also tried. The result for argon is illustrated in Fig. 19. In both cases, the gas was introduced into the cavities at about  $10^{-4}$  to  $10^{-5}$  Torr and RF processing proceeded at moderate level (corresponding to about 100 MV/m peak

field). After pumpdown,  $j_F$  was found to be somewhat lower than before "scrubbing," but the value of  $\beta$  remained essentially unchanged, and the ultimate breakdown field did not increase. It should be noted, however, that these "RF scrubbing" experiments were done after the cavities had undergone many hours of RF processing in vacuum and the disk edges were already considerably pitted.

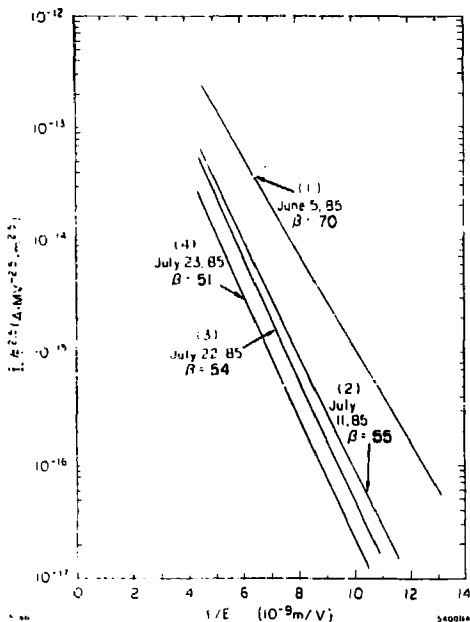


Fig. 19. RF Fowler-Nordheim plots for S-band (seven-cavity,  $2\pi/3$ -mode) structure as a function of time. Curve (4) was recorded shortly after argon scrubbing and pumpdown.

#### Confrontation of Results with Existing Models

The measurements and observations presented here must now be examined in the light of existing models for field emission and breakdown.

Models for field emission fall into two basic categories. The first is based on the original Fowler-Nordheim theory [Eqs. (4-7)] in which the rate of electron tunneling through a potential barrier at the metal-vacuum interface is affected only by the metal work function and the external electric field. This field, however, to make the observed emitted currents consistent with observations, must be "enhanced" by a factor  $\beta$  which depends on surface geometry, typically sharp peaks, cracks, whiskers or micro-protrusions. A number of workers have either observed or postulated such protrusions and have calculated  $\beta$ -values as high as 1000 from Fowler-Nordheim plots. (In this area there is a voluminous amount of literature; see, for example, Refs. 10, 11, 15, 16, 17 and 18.) For the sake of simplicity, we shall call this the "mountain" model. In recent years, the pure "mountain" model has fallen into partial disfavor because few optical observations have revealed "peaked" enough mountains to explain the data. This observation is certainly true in our case: we do not see metal surface irregularities which can explain the  $\beta$ -values of  $\sim 60$  measured in our S-band cavities or even  $\sim 40$  in our C-band cavities.

The second theory<sup>11,12,20</sup> assumes surface oxides, adsorbed organic residues, dielectric inclusions on the surface or between

crystal boundaries, dust, etc. For succinctness we shall call this the "snow" model, in analogy with layers of snow on the mountains. The externally applied electric field penetrates into this intermediate dielectric layer and accelerates the electrons from the Fermi level in the metal. This acceleration is equivalent to heating up the electrons, thereby called "hot electrons," which can then escape into the vacuum through a quasi-thermionic process, following the old Richardson-Dushman model. Several variations of the "hot electron" theory are presently being considered, of which the principal is the FIHEE (Field-Induced Hot-Electron Emission) model<sup>11,12,20</sup>. Where the Richardson-Dushman model is invoked, the emitted current density is given by:

$$j_F = K T_e^3 \exp(-e\chi/kT_e) A/m^2 \quad (11)$$

where  $\chi$  is the height of the surface potential barrier,  $K$  is a constant ( $\sim 1.2 \times 10^{-6} \text{ Am}^{-2}$ ),  $k$  is Boltzmann's constant and the energy of the hot electrons is measured by the kinetic energy they acquire in the dielectric layer of width  $\Delta d$  and of relative dielectric constant  $\epsilon$ :

$$\frac{3}{2} kT_e = \frac{eE}{\epsilon} \Delta d \quad (12)$$

The average RF current density analogue to Eq. (5) is then:

$$j_F = 3.89 \times 10^{-6} K \left[ \frac{2e\Delta d}{3k\epsilon} \right]^2 E^{3.5} \exp \left\{ -\frac{3\chi\epsilon}{2\Delta d E} \right\} A/m^2 \quad (13)$$

By comparison, an effective  $\beta_{eff}$  can be obtained:

$$\beta_{eff} = 4.353 \times 10^9 \phi^{1.5} \frac{\Delta d}{\chi\epsilon} \quad (14)$$

Assuming  $\phi = 4.65 \text{ eV}$ ,  $\chi = 4 \text{ eV}$  and  $\Delta d$  measured in nanometers, we see that

$$\beta_{eff} = 10.9 \frac{\Delta d}{\epsilon} \quad (15)$$

Thus, for example, for a  $\beta_{eff}$  of 60 and  $\epsilon = 3$ ,  $\Delta d$  comes out to be 16.5 nm (in slight disagreement with Ref 10). This calculation assumes that the metal surface is perfect and that the entire  $\beta_{eff}$  can be ascribed to the dielectric of thickness  $\Delta d$ . In actual fact, perfect machining does not exist and even before the cavities are damaged by breakdown and sparking, there is a contribution to the value of  $\beta$  due to metal surface imperfections. After multiple breakdowns, let us assume that the surface damage seen in Fig. 18 explains  $\beta_1$ 's of magnitude 6 and that a multiplicative  $\beta_2$  of magnitude 10 due to a dielectric layer gives a total  $\beta_{eff} = \beta_1\beta_2 = 60$ . Using the same parameters as in Eq. (15), we then find that the  $\Delta d$  layer on the damaged metal surface is on the order of 2.8 nm.

Although we have no direct measurements of these respective layer thicknesses, they are at least plausible. When we begin an RF processing cycle, the evidence is that the internal cavity surfaces are indeed covered with impurities and that the FE currents at a given field level are comparatively high. As electron and photon bombardment proceeds and gas desorption and pumpdown take place, FE decreases and seems to reach an asymptotic lower level.

Unfortunately, we do not have an evolutionary measurement of  $\beta$  during the RF process. The reason is that until a cavity has been RF processed to the point where it operates at its asymptotic field (either through successive breakdowns or through "RF scrubbing" with argon), a single-valued and accurate Fowler-Nordheim plot over a reasonable range of  $1/E$  cannot be obtained. By the time the total range of fields can be scanned without breakdown, the impurities are desorbed to a substantial degree and the surface damage from multiple breakdown events is already irreversible. The measured  $\beta$  is then the final  $\beta$ .

That this scenario is approximately correct can also be concluded from our observation that after our S-band two-cavity structure was exposed to CO, the FE current was at first increased. However, as pointed out earlier, after 15 to 30 minutes of RF processing (i.e., of "snow" removal) it returned to its pre-exposure level, i.e., the few mono-layers were desorbed.

Now let us focus on the breakdown process. In contrast to field emission, which is a relatively steady and reproducible process, breakdown is a catastrophic phenomenon. As with many such phenomena, we seem to be able to list the general conditions which lead to it, but we are not able to predict the exact time when and exact location where it takes place. The consensus<sup>10,21,22,23</sup> is that the ultimate type of breakdown, i.e. the one that invariably damages the surface, is due to Explosive Electron Emission (EEE).

The general model for EEE is that the local effective electric field at a particular surface site reaches a level such that the FE current raises its temperature to the melting point. Instantaneous melting and evaporation of metal and inclusions take place, the gas rapidly expands and gets ionized into a plasma, light is emitted, the surface is irreversibly deformed and the condition of the initial site is changed. The local field emitted current drops off and the breakdown stops. The entire phenomenon resembles a volcanic eruption.

To be more specific, let us consider that the local field at a site reaches 8-9 GV/m. In this range, the FE current density is on the order of  $10^8$ - $10^9$  A/cm<sup>2</sup>. The heat dissipation per cm<sup>2</sup> through ohmic loss from such a current in a medium of resistivity  $\rho$  is then  $\bar{j}^2 \rho$ . If we assume to first order that this heat does not have the time to be conducted away, it will raise the temperature of the volume by  $\Delta T$  (°C) in a time

$$\Delta t = \frac{4.18 MC \Delta T}{\bar{j}^2 \rho} \quad (16)$$

where  $M$  is the density in grams/cm<sup>3</sup>,  $C$  is the heat capacity per gram, and  $\rho$  is measured in ohms-cm. As it turns out, the time to reach the melting point of the metal does not depend very much on which metal is considered (in agreement with the results of Ref. 6.) and is roughly equal to:

$$\Delta t = \frac{2 \times 10^9}{\bar{j}^2} \text{ seconds} \quad (17)$$

Thus, for  $\bar{j} = 10^9$  A/cm<sup>2</sup>,  $\Delta t \sim 2$  nsec. This result is consistent with our observations (Fig. 10) and that of other reports that breakdown, on the microsecond scale, is essentially instantaneous. In our case, i.e. pulsed RF, all subsequent observations as we reported them above, are consistent with the model, i.e. we witness:

- a large current jump (by a factor of 20-30) due to the ionization of the plasma and the release of electrons,
- emission of light (the cathode flare or spark reported by others),
- a sudden power reflection from the structure (due to the consumption of a significant fraction of the few joules stored in the cavity and the collapse of the fields),
- a sudden rise in carbon-related molecules in the RGA (the evaporated copper is too heavy to reach the RGA and is locally reabsorbed by the cold walls of the cavity),
- that the cavity disks, upon subsequent examination, are damaged.

#### Remaining Problems and Conclusions

Having convinced ourselves that our scenario of "snow covered mountains" sometimes subject to "volcanic eruptions" is a rather plausible one, let us now conclude by listing a few problems that still need to be resolved through further work:

1. In our S-band structures, breakdown first appeared at  $\sim 86$  MV/m in the seven-cavity section and at  $\sim 170$  MV/m in the somewhat cleaner two-cavity structures. Both were processed up to over 300 MV/m peak field. Did the early breakdown events, predominantly due to "snow," cause surface damage? We believe so but we did not examine the inside of the cavities until we reached the top field. By that time, there were plenty of "mountains" and "craters" formed.
2. Close to the top field, immediately after a breakdown event, the FE current generally returns exactly to its pre-breakdown level. What does this mean? Why doesn't the modification of the one local mountain with its local snow change the FE current? Probably because by this time, there are many similar sites, which combined with the production of numerous other secondary emitted electrons, swamp the effect of the local change.
3. We observed throughout our experiments that the FE current was independent of the pressure in the cavity, a fact which is consistent with the above model. The probability of breakdown occurrence was also quite pressure-independent in the  $10^{-8}$  to  $10^{-6}$  Torr range. When the pressure at the pumps approaches  $10^{-6}$  Torr, the frequency of breakdown does increase and the measurements become somewhat unstable. It must be stated that the exact pressure in our cavities subject to breakdown is not known because the pumps (see Fig. 7) are about a meter or so away, and local puffs of gas ("clouds" over the mountains) cannot be measured accurately; they can only be inferred. Thus it is possible that the ultimate breakdown trigger is caused by a local instability or runaway condition, ion formation (à la Kilpatrick!) with extra surface bombardment, sudden space charge neutralization which raises the local field, or even a more complex phenomenon. Thus to carry our geophysical analogy one step further, it may be that the volcanic eruption of a snow-covered mountain is finally precipitated by the cloud floating above it.
4. This brings us to the next question: why does the breakdown field vary as  $f^{1/2}$ , in basic agreement with the Kilpatrick formula, even though we showed earlier that his model does not seem to apply to our high frequency case? One possibility is that the ions, whose energy does vary as  $f^{-2}$  (see Eq. 9), do play a role in triggering the breakdown after all. Another proposed idea<sup>24</sup> is that the frequency dependence has something to do with a required buildup time of the hot-electron population. The shorter the time becomes, the less the full enhancement can materialize. According to J. Halbritter, there might result a saturation in the field emission due to the neutralization of positive charges in the dielectric interface. This theory, however, is still speculative and requires further confirmation.
5. Finally, we have to ask ourselves if there is some way of suppressing or at least controlling the field emission and the breakdown in an actual extremely high-gradient accelerator. The field emission is detrimental because it can absorb a substantial fraction of the RF energy, cause wakefields and x-ray radiation, and, if captured over a long accelerator length, may be hard to separate from the real beam. The breakdown is detrimental for obvious reasons: it interrupts the operation of the machine, it damages the structure, and through the formation of surface defects, it increases or at least creates a high level of asymptotic field emission.

Since surface contamination of one sort or another during the manufacturing process is probably inevitable, RF processing will undoubtedly be needed to clean up the internal surfaces of the accelerator. The question is then:

can this be done without damage to the surface, thereby ending up with a  $\beta$  of  $\sim 10$  rather than 80? The answer is that it may be possible to avoid surface damage by starting out with argon or helium processing, or treatment with another gas such as atomic oxygen. We are presently thinking of experiments to check out these ideas.

#### Acknowledgements

Over the past four years since these RF breakdown studies started at SLAC, many people assisted the authors in various phases of the work. J. Zamzow helped with all the high power waveguide installations, the vacuum system and the gas exposure tests. H. Deruyter gave his assistance in many of the RF cold tests. P. Corredoura set up the VAX-785 computer interface system to digitize and record the breakdown pulses. H. Hoag led the mechanical design and construction of the recent 11.42 GHz traveling-wave section. E. Hoyt helped with many useful discussions regarding surface damage, gas exposures, and provided the scanning electron microscope pictures of the breakdown in copper. V. Nguyen-Tuong, while visiting SLAC, was the prime mover in the tests involving argon processing. R. Ecken and G. Aske were helpful in improving the operation of the test stand and C. Griffin managed to "squeeze" 47 MW out of an old 36 MW XK-5 klystron. Excellent support was received from the SLAC shops, in particular from D. Fuller, J. Pope, D. Wright, W. Jacopi, O. Millican and D. Sartain. R. McCall, T. Jenkins, R. Nelson, D. Busick S. Carlson, D. Walz and N. Ipe helped with the radiation and beam energy calculations and measurements, and K. Brown with beam transport calculations. Last but not least, very useful overall discussions were held with R. Miller, E. Garwin, R. Kirby, A. Schwetman and J. Halbritter. E. Tanabe from Varian was our collaborator in the planning and tests of C- and X-band half-cavities performed at Varian. Valuable assistance at Varian was also given by L. Nelson and F. Gordon.

A special acknowledgement is due Dr. Renzo Parodi from the I.N.F.N. in Genova, Italy, who took a personal interest in calculating and plotting field-emitted electron trajectories with his NEWTRAJ computer program, of which one example appears in this paper.

The authors are indebted to all the above individuals as well as to B. J. Ferandin, K. Johnston and the SLAC Publications Department for preparing this and earlier reports.

#### References

1. R. B. Palmer, "The Interdependence of Parameters for TeV Linear Colliders," presented at the Workshop on New Developments in Particle Accelerator Techniques, Orsay, France, June 1987, SLAC-PUB-4295, April 1987.
2. J. W. Wang and G. A. Loew, "Measurements of Ultimate Accelerating Gradients in the SLAC Disk-loaded Structure," presented at the 1985 Particle Accelerator Conference, Vancouver, B.C., May 1985, SLAC-PUB-3597, March 1985.
3. J. W. Wang, V. Nguyen-Tuong and G. A. Loew, "RF Breakdown Studies in a SLAC Disk-loaded Structure," Proceedings of the 1986 Linear Accelerator Conference, Stanford, CA, June 1986, SLAC-PUB-3940, April 1986.
4. J. W. Wang and G. A. Loew, "Progress Report on New RF Breakdown Studies in an S-band Structure at SLAC," presented at the 1987 Particle Accelerator Conference, Washington, D.C., March 1987, SLAC-PUB-4247, February 1987.
5. E. Tanabe, J. W. Wang and G. A. Loew, "Voltage Breakdown at X-band and C-band Frequencies," Proceedings of the 1986 Linear Accelerator Conference, Stanford, CA, June 1986.
6. E. Tanabe, "Breakdown in High-Gradient Accelerator Cavities," Proceedings of the 1984 Linear Accelerator Conference, Seeheim/Darmstadt, West Germany, p. 403.
7. M. A. Allen, et al., "Relativistic Klystron Research for High Gradient Accelerators," presented at the European Particle Accelerator Conference, Rome, Italy, June 1988, SLAC-PUB-4650, June 1988.
8. G. A. Loew, "Considerations of RF Frequency and Power Generation in Linear Colliders Using 'Conventional' Technology," SLAC-AAS-22, October 1986.
9. R. B. Palmer, "Advanced Concepts for Particle Accelerators," presented at the European Particle Accelerator Conference, Rome, Italy, June 1988.
10. See for example, R. V. Latham in "High Voltage Vacuum Insulation: The Physical Basis," Academic Press, 1981, pp. 53-54.
11. R. V. Latham, "Prebreakdown Electron Emission," IEEE Trans. Elec. Insul., Vol. EI-18 No. 3, June 1983, pp. 194-203.
12. J. Halbritter, "On Contamination on Electrode Surfaces and Electric Field Limitations," IEEE Trans. Elec. Insul., Vol. EI-20 No. 4, August 1985, pp. 671-681.
13. W. D. Kilpatrick, "Criterion for Vacuum Sparking Designed to Include Both RF and DC," Rev. of Sci. Instrum. 1957 Vol. 28, No. 10, pp. 824-826.
14. Calculations carried out by Dr. Renzo Parodi, INFN, Genoa, Italy, in collaboration with this program.
15. R. P. Little and W. T. Whitney, "Electron Emission Preceding Electrical Breakdown in Vacuum," J. Appl. Phys. 34, August 1963, pp. 2430-2432.
16. I. Brodie, "Studies of Field Emission and Electrical Breakdown Between Extended Nickel Surfaces in Vacuum," J. Appl. Phys. 35, August 1964, pp. 2324-2332.
17. D. Alpert, et al., "Initiation of Electrical Breakdown in Ultrahigh Vacuum," J. Vacuum Sci. and Technol. Vol. 1 (1964), pp. 35-50.
18. R. J. Noer, "Electron Field Emission from Broad-Area Electrodes," Appl. Phys. A 28 (1982).
19. G. Ecker, "Review of Present Understanding of Electrode Phenomena," IEEE Trans. Elec. Insul., Vol. EI-18 No. 3, June 1983, pp. 243-252.
20. R. V. Latham, "Prebreakdown Electron Emission Processes," Proceedings XIIIth Int. Symp. on Discharges and Electrical Insulation in Vacuum (1986), pp. 15-30.
21. G. A. Mesyats, "Explosive Processes on the Cathode in a Vacuum Discharge," IEEE Trans. Elec. Insul., Vol. EI-18 No. 3, June 1983, pp. 218-225.
22. E. A. Litvinov, "Theory of Explosive Electron Emission," IEEE Trans. Elec. Insul., Vol. EI-20 No. 4, August 1985, pp. 683-689.
23. J. N. Fursey, "Field Emission and Vacuum Breakdown," IEEE Trans. Elec. Insul., Vol. EI-20 No. 4, August 1985, pp. 659-670.
24. J. Halbritter, "Dynamical Enhanced Electron Emission and Discharges at Contaminated Surfaces," Appl. Phys. A 39, (1986) pp 49-57.

## **DISCLAIMER**

This report was prepared as an account of work sponsored by an agency of the United States Government. Neither the United States Government nor any agency thereof, nor any of their employees, makes any warranty, express or implied, or assumes any legal liability or responsibility for the accuracy, completeness, or usefulness of any information, apparatus, product, or process disclosed, or represents that its use would not infringe privately owned rights. Reference herein to any specific commercial product, process, or service by trade name, trademark, manufacturer, or otherwise does not necessarily constitute or imply its endorsement, recommendation, or favoring by the United States Government or any agency thereof. The views and opinions of authors expressed herein do not necessarily state or reflect those of the United States Government or any agency thereof.